Noise Model of a Multispectral TDI CCD Imaging System and Its Parameter Estimation of Piecewise Weighted Least Square Fitting

Liangliang Zheng, Guang Jin, Wei Xu, Hongsong Qu, and Yong Wu

***Abstract*— The time-delayed integration (TDI) charge-coupled device (CCD) imaging technology is widely used in remote sensing field and accurate estimation of noise level is essential to assure good performance of denoising. Therefore, in order to achieve images with high signal-to-noise ratio by the TDI CCD sensor, the noise model of the imaging system is investigated. First, the design of the imaging circuit system is presented, and the main noises of the system are analyzed, such as the TDI CCD sensor, amplifiers, and so on. Then a theoretical noise model of the imaging system is established as *a priori* information. An improved least square fitting method of parameter estimation is proposed. To validate the theoretical model and the proposed method, extensive tests are carried out to obtain multiple uniform images on a developed TDI CCD imaging system. The experiment results confirm that a precise noise model can be achieved by this method and it verifies the theoretical model, meanwhile. It can be used for noise removal and aided design of imaging systems to acquire high-quality images. It is meaningful for remote sensing to obtain more targets of interest.**

***Index Terms*— Noise model, time-delayed integration (TDI), charge-coupled device (CCD), imaging system, parameter estimation.**

I. Introduction

UNLIKE conventional charge-coupled device (CCD), the time-delayed integration (TDI) CCD is a kind of linear array photoelectric detector, which implements charge accumulations by superposition mode. Based on this principle, it has advantages, such as high sensitivity, high dynamic range and low noise, making it widely used in aerospace, remote sensing, measurement and other fields. Especially in remote sensing field, it can reduce the relative aperture of optical systems, which can make the space camera lighter and smaller.

Many image processing algorithms such as denoising, compression and segmentation, etc., take noise level as an input parameter [1]. Accurate noise level estimation is essential to assure good performance of each processing procedure [2]. Therefore, to achieve image data with high signal-to-noise ratio(SNR) in earth observation fields, we investigate the noise model of a TDI CCD imaging system in this paper. It(The proposed model) can be practically not only applied to denoise the digital images captured by TDI CCD, further to enhance their quality, but also used for aided design of TDI CCD imaging circuit systems.

Some papers have proposed or analyzed the noise model for CCD or CMOS imaging systems [2], [7], [10], [11], [13], [15]–[19].

It is usually assumed that the noise characteristics are the additive white Gaussian noise(AWGN), used to denoise the image data [1], [3], [4]. However, besides the AWGN, there are other types of noise, e.g., signal-dependent noise, which is dominant when the video signal is stronger [2], [7], [10], [11], [13], [15]–[19].

The imaging system outputs the raw image data. The noise model of the raw image is described by a function that is given the intensity of a pixel in the noisy image returning the corresponding variance, also called a noise level function(NLF), in [5] and [6]. It is a linear continuous function describing the noise level as a function of image brightness. The plot of this function is the noise curve [7].

There is some research work on the noise of TDI CCD sensor. It can be usually divided into two categories, one is the inherent noise, including photon shot noise, dark current, fixed pattern noise and transfer noise, etc.; the other is all kinds of interference noise, such as reset noise and 1/f noise, etc., [8], [9].

Once we derive a noise model, a priori information, the next step to establish a practical model turns out to be a question of parameter estimation. This challenging problem has been extensively studied by researchers. There are mainly two routes for noise estimation. One is from a single image, and the other is based on multiple images. The former applies discrete cosine transform(DCT) or discrete wavelet transform(DWT), etc., in orthogonal transform domain, to achieve the necessary information by removing possible structures from a single image in [10] and [11]. Then the maximum-likelihood(ML) approach [5], [6], [10], [11], and least square(LS) fitting or polynomial [11] are exploited to derive the practical model. The latter directly employs LS [2], [12], [13], ML [14] or interpolation, etc., in spatial domain, to obtain the practical model in terms of the multiple uniform images [15].

Estimation from a single image is an underconstrained problem and further assumptions have to be made for the noise [5]. Estimation from multiple images, however, is an

Manuscript received March 29, 2017; accepted April 18, 2017. Date of publication April 24, 2017; date of current version May 22, 2017. This work was supported by the National 863 Plan Project of China under Grant 2012AA121502. The associate editor coordinating the review of this paper and approving it for publication was Dr. Shoushun Chen. *(Corresponding author: Liangliang Zheng.)*

The authors are with the Changchun Institute of Optics, Fine Mechanics and Physics, Chinese Academy of Sciences, Changchun 130033, China (e-mail: adqe@163.com; jing@ciomp.ac.cn; xwciomp@126.com; quhongsong@aliyun.com; wuyongjlu@163.com).

Digital Object Identifier 10.1109/JSEN.2017.2696562

overconstrained problem and was addressed in [15]. The single image content is certainly non-uniform and may include different texture patterns, edges, objects of small size, etc. All these heterogeneities will influence the performance of a noise parameter estimator, which lead it hard to realize a robust and stable fit, described in [10] and [11]. The procedures of transformation and processing to achieve the necessary information are possibly complex. By contrast, noise estimation based on multiple uniform images can implement a robust fit and the procedure is simpler. Although it is time consuming to obtain images covering the full intensities, it is an essential procedure to develop a high-performance camera, which is an indispensable experiment for airborne or space-borne imaging systems.

In this work, the theoretical noise model of TDI CCD imaging systems is established as a priori information according to the design of imaging circuit systems. An improved least square fitting method of parameter estimation is proposed. Sufficient experiments are conducted on the developed imaging system using a TDI CCD sensor, capable of panchromatic and multi-spectral photosensitivity. The accurate noise model for the whole imaging system, i.e., the NLF, is derived by multiple images. The theoretical noise model is verified and the effectiveness of our parameter estimation algorithm is demonstrated.

The rest of the paper is organized as follows: after reviewing the relevant work in section II, we describe the design of TDI CCD imaging circuit system and establish the theoretical noise model in section III. Section IV proposes the improved method of parameter estimation and section V analyzes the data sets of experiments to validate the theoretical model and the proposed algorithm. The conclusion is presented in section VI.

II. Related Work

In this section, we briefly review previous work on noise models of imaging system and the methods of parameter estimations.

A. The Noise Model of Imaging System

The raw image *y(t,s)* in [10] is supposed as the following model, which is affected by the signal-dependent noise:

$$y(t,s) = x(t,s) + n[t,s,x(t,s)]. \tag{1}$$

In which, $t = 1 \ldots N_c$, $s = 1 \ldots N_r$, an image is denoted with N_c columns by N_r rows, *x(t,s)* is the original noise-free image, *n[t,s,x(t,s)]* is an ergodic Gaussian noise with zero mean, signal-dependent variance $\sigma_n^2[x(t,s)]$ and a 2-D Dirac delta function for its spatial autocorrelation function. For a general case, for signal-dependent noise variance $\sigma_n^2(I)$, we assume a polynomial model with degree n_p: $\sigma_n^2(I,c) = c \times [1, I, I^2, \cdots, I^{n_p}]$, where I is the true image intensity and $c = (c_0, c_1, \cdots, c_{n_p})$ is a coefficient vector with size $(n_p + 1) \times 1$.

However, a reduced-order noise model is focused on for recent CCD sensors. In this case, the noise *n[t,s,x(t,s)]* is supposed to be the sum of two components: $n[t,s,x(t,s)] = n_{SI}(t,s) + n_{SD}[t,s,x(t,s)]$. The first one, $n_{SI}(t,s)$, is signal-independent with variance $\sigma_{n.SI}^2$, and the second one, $n_{SD}[t,s,x(t,s)]$, is signal-dependent with variance $\sigma_{n.SD}^2 \times I$(Poisson-like noise). This corresponds to a polynomial model of the first order ($n_p = 1$) and, thus the coefficient vector simply reduces to $c = (\sigma_{n.SI}^2, \sigma_{n.SD}^2)$:

$$\sigma_n^2(I) = \left(\sigma_{n.SI}^2, \sigma_{n.SD}^2\right) \cdot [1, I] = \sigma_{n.SI}^2 + \sigma_{n.SD}^2 \cdot I. \tag{2}$$

Simplified by parameters a and b, it can be described by:

$$\varphi(\mu) = \sigma^2 = a \times \mu + b. \tag{3}$$

In which μ is the expectation of the intensity of this pixel in the noisy image. This model is valid under the assumption that the signal is not saturated. At the darkest pixels, the Poisson distribution of the noise cannot be approximated by a Gaussian and it becomes a shot noise. For most CCDs and CMOS detectors, the variance of the noise at a pixel can be approximated by this linear model [2], [11], [13], [16]–[18].

B. The Method of Parameter Estimations for Noise Models

Parametric estimation methods for noise model try to obtain the parameters that control the noise model, for example, parameters a and b in the linear model (3). There are different parameter estimation strategies, such as the maximum-likelihood(ML), least square(LS) and weighted least square(WLS), etc.

The ML approach employs the probability density function(PDF) to estimate the parameter applied in [10], [11], and [14]. For the samples $\{\hat{\mu}_i, \hat{\sigma}_i\}_{i=1}^N$, which are the estimates of the intensity and its standard deviation in [11], the PDFs of $\hat{\mu}_i$ and $\hat{\sigma}_i$ given $\hat{\mu}_i = \mu$ are respectively supposed to be:

$$f_1(\hat{\mu}_i | \mu_i = \mu) = \frac{1}{\sqrt{2\pi\sigma_{reg}^2(\mu)c_i}} e^{-\frac{1}{2\sigma_{reg}^2(\mu)c_i}(\hat{\mu}_i - \mu)^2}$$

$$f_2\left(\hat{\sigma}_i \mid \mu_i = \mu\right) = \frac{1}{\sqrt{2\pi\sigma_{reg}^2(\mu)d_i}} e^{-\frac{1}{2\sigma_{reg}^2(\mu)d_i}\left(\hat{\sigma}_i - \sigma_{reg}(\mu)\right)^2},$$

where $\sigma_{reg}^2(\mu)$ is defined as a simple regularized variance-function; c_i and d_i are known coefficients in [11]. Hence the PDF is $f((\hat{\mu}_i, \hat{\sigma}_i)|\mu_i = \mu) = f_1(\hat{\mu}_i|\mu_i = \mu) \times f_2(\hat{\sigma}_i|\mu_i = \mu)$. The posterior likelihood function L is obtained by considering all measurements $\{\hat{\mu}_i, \hat{\sigma}_i\}_{i=1}^N$ and by integrating the densities f:

$$L(a,b) = \sum_{i=1}^{N} \int_{-\infty}^{\infty} f\left((\hat{\mu}_i, \hat{\sigma}_i)|\mu_i = \mu\right) d\mu.$$

The parameter estimates $\hat{a}$ and $\hat{b}$ are obtained from the solution of the following equation:

$$\left(\hat{a}, \hat{b}\right) = \arg\max_{a,b} L(a,b) = \arg\min_{a,b} -\mathrm{In}L(a,b). \tag{4}$$

The difficulty of ML approach usually lies in that the PDF is hard to obtain and the solving process is slightly complicated.

The LS fitting, a widely used estimation method, is to seek a function of $\varphi(\mu)$ in data sets to minimize the sum of squared error(SSE) employed in [11] and [13]. Here we exploit this

method to find a first-order polynomial $\varphi(\mu)$, expressed as (3), in measurements $\{\hat{\mu}_i, \hat{\sigma}_i\}_{i=1}^N$ to make the SSE minimum:

$$\left(\hat{a}, \hat{b}\right) = \arg\min_{a,b} \sum_{i=1}^{N} [\varphi\left(\hat{\mu}_i\right) - \hat{\sigma}_i^2]^2. \tag{5}$$

The WLS method, improved based on LS, utilizes weighted factors to minimize the SSE, which can further diminish the error between the actual value and the estimated one to realize a better fit. Meantime, it can reduce the heteroskedastic influence effectively. For WLS, (5) is changed into:

$$\left(\hat{a}, \hat{b}\right) = \arg\min_{a,b} \sum_{i=1}^{N} W_i[\varphi\left(\hat{\mu}_i\right) - \hat{\sigma}_i^2]^2, \tag{6}$$

where W_i is the weighted factor.

It has been applied in [12], which took into account the number of points in clusters to calculate the weighted factor W_i. For each cluster $C_{cli}, i = 1, \ldots, N_{cl}$, the W_i is defined as:

$$W_i = N_{cli} / \sum_{m=1}^{N_{cl}} N_{clm}, \tag{7}$$

where N_{cli} determines the number of points in the cluster C_{cli}. It was proved that this weighted algorithm could provide considerable improvement in the accuracy of line fitting and better estimation of the parameters [12].

For a variable U with its samples $\{\mu_i\}_{i=1}^N$, which obeys the normal distribution, i.e., $U \sim N(\mu, \sigma^2)$, where μ and σ^2 are the expectation and variance of U, respectively, we can employ ML approach to derive the estimations of μ and σ^2:

$$\begin{cases} \hat{\mu} = \dfrac{1}{N} \sum_{i=1}^{N} \mu_i = \bar{U} \\ \hat{\sigma}^2 = \dfrac{1}{N} \sum_{i=1}^{N} (\mu_i - \bar{U})^2. \end{cases} \tag{8}$$

Using (8), we can calculate the local estimations of the expectation and standard-deviation(STD) pairs from the data sets.

III. Theoretical Noise Model of TDI CCD Imaging System

In this section, the design principle of TDI CCD imaging circuit system is presented, in terms of which the relevant main noises are analyzed and the theoretical noise model is established.

A. Design of TDI CCD Imaging Circuit System

The imaging system is performed around the centre of TDI CCD sensor. It can convert the light signals of objects into digitalized electrical signals that we can observe and analyze to obtain the useful information acquired by dedicated devices.

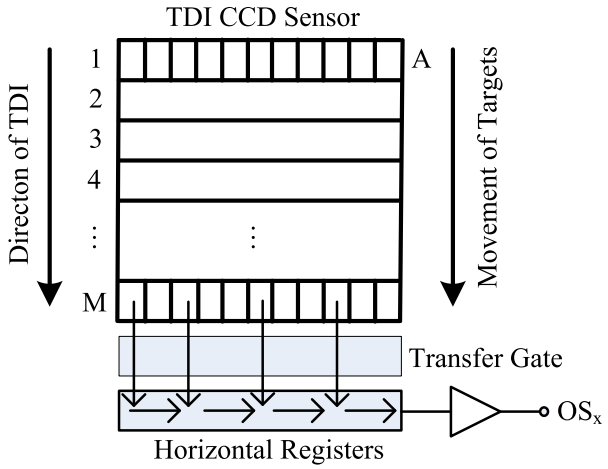

Fig. 1. Illustration of TDI CCD working principle.

1) TDI CCD Sensor: TDI CCD is a kind of special linear array CCD detector, which can execute repeated exposure to the same target by adopting superposition scan mode [8]. Its working principle is that, for M TDI stages, integrating charges of objects are adding M number of lines together. Fig. 1 is the illustration of TDI CCD working principle. When a target A is moving along the direction of TDI toward the stage of M, the first row completes the exposure of target A during integration time, then the exposure charges of the first row are transferred to the second row, simultaneously target A moving to the second row. The second row continues the exposure of target A, so the charges of 'A' are added by two times. This operation is continuously repeated until the charges reach the last row of M. The accumulated charges will be M times as much as a single line, and they will be read out by horizontal driving signals when the transfer gate is open, which are finally output in the form of analog voltages from the port of OS_x. The TDI principle is particularly significant at low light level operations since the exposure time can increase with the number of the TDI stages, which makes the sensor practical for remote sensing applications.

2) Design of Imaging Circuit System: The imaging circuit system can fulfill the driving of TDI CCD sensors, the supply of power, quantization of the video signal and outcome of the image data. It usually comprises TDI CCD sensor, amplifiers, video processors, power circuits, driving circuits and digital processing circuit, etc., as shown in Fig. 2.

The light signals of objects irradiate on the focal plane array of TDI CCD, performing integral exposure and producing analog video signals of the targets. The amplifiers, protecting the sensor from unexpected tests, can match the impedance, enlarge the video signals at a proper ratio and lead them to the video processors, which integrate correlated double sampling(CDS) module, programmable gain amplifier(PGA) and analog-to-digital converter(ADC). Their main functions are to extract the effective signal, amplify and quantify the analog signals into digital ones. They are one of the key links that affect the SNR of images. Then the digital image is sent to the buffers of a digital processing circuit, the control kernel of the imaging circuit system. This circuit

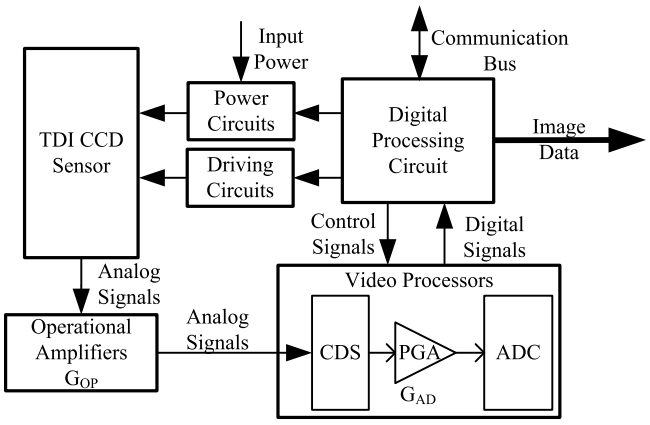

Fig. 2. Sketch map of TDI CCD imaging circuit system.

is primarily responsible for outputting the primitive driving signals that meet the requirements of CCD sensor, controlling the start-up and turn-off sequences of bias voltages and the working sequence of the video processors. By means of the communication bus, the digital processing circuit receives the commands and returns the state parameters. Moreover, it can integrate the image data and output it as an agreed format through high speed interfaces. The driving circuits serve for the sensor, amplifying the primitive CCD driving signals and outputting multiple signals according to the desired working sequence. The power circuits provide a variety of stable bias voltages to TDI CCD. Both circuits are the key parts to the quality of images acquired by the system.

3) Response of Imaging System: According to the principle of photoelectric conversion of CCD in [20], the output voltage of the TDI CCD sensor is given by:

$$V_S = E(\lambda) M T_{INT} R(\lambda). \tag{9}$$

In which $E(\lambda)$ is the illumination irradiated onto the surface of the sensor, whose unit is W/m^2. λ is the average wavelength of the incident light. M expresses the integration stage of TDI CCD and its range of values is up to the structure of the sensor itself. T_{INT} is the integration time. $R(\lambda)$ indicates the spectral response function, which shows the ability of photoelectric conversion. It is the key parameter to the sensor and its unit is V/μJ/cm^2.

According to the signal process of the imaging system, shown in Fig. 2, its output is in digital number(DN). So the output data of the system can be expressed as:

$$V_{DN} = G_{OP} G_{AD}\, kE(\lambda) M T_{INT} R(\lambda), \tag{10}$$

where G_{OP} and G_{AD} are the gain of the amplifiers and the video processor, respectively. k represents the quantification ratio of analog to digital number, up to the video processor. For an ADC with the maximum quantized voltage V_{max}, we can get the parameter k:

$$k = (2^n - 1) \big/ V_{max},$$

where n indicates the number of quantization bits. The output of the ADC is described by DN, an integer with the range of [0,2^n-1].

For a multispectral TDI CCD imaging system with panchromatic(P), red(R), green(G) and blue(B) spectrums, the response can be calculated by:

$$\begin{cases} V_{DNP} = G_{OPP} G_{ADP} k E_P(\lambda) M_P T_{INTP} R_P(\lambda) \\ V_{DNR} = G_{OPR} G_{ADR} k E_R(\lambda) M_R T_{INTB} R_R(\lambda) \\ V_{DNG} = G_{OPG} G_{ADG} k E_G(\lambda) M_G T_{INTB} R_G(\lambda) \\ V_{DNB} = G_{OPB} G_{ADB} k E_B(\lambda) M_B T_{INTB} R_B(\lambda), \end{cases} \tag{11}$$

where the subscript letters express the variables of specific spectrum. The integration time for R, G and B spectrums is the same, expressed as T_{INTB}.

B. Theoretical Noise Model of Imaging System

The noises of different components in the imaging system are discussed in this part. The theoretical model is derived.

1) Noise of TDI CCD Sensor: There are a variety of noises in the output signal of TDI CCD, such as photon shot noise, dark current noise, fixed pattern noise (FPN), reset noise, 1/f noise, etc.

a) Photon shot noise: The process of generating signal charges with light inputting the TDI CCD photosensitive area can be considered as an independent, uniform, continuous occurring random process, and photon shot noise characterizes the uncertainty in the number of signal charges stored at a collection well, which is a fundamental limitation and cannot be eliminated [15]. This number of charges follows a Poisson distribution so that its variance equals its mean:

$$\sigma^2_{photon} = N_s, \tag{12}$$

where N_s is the mean charge number of the sensor [8], [15].

b) Dark current noise: The dark current is an intrinsic noise to CCD. It is due to the thermal excitation of electrons into the conduction band and collection in the CCD wells, generated even though the sensor is not exposed to light. The dark current signal depends approximately exponentially on the temperature and linearly with exposure time. Its generation is a statistical process described by the Poisson distribution [21], [22].

In the application of TDI CCD, taking thermal control measures and adopting short integration time, often in microseconds, will effectively reduce the dark current noise.

c) FPN: The difference of integral position and readout path of each signal charge packet contributes to small variations in each charge packet, often called fixed pattern noise(FPN). The FPN does not change with time and space, so it can be separated and removed [8], [15].

d) Reset noise and 1/f noise: The reset noise(also called thermal noise) is caused by the reset switch of readout amplifier circuit, which sequentially transforms the charge collected into a measurable voltage. The 1/f noise, which is also termed as the flicker noise, originates in the amplifier part of the circuit [9], [15]. Between both noises, the main one is the reset noise originating mainly from the floating diffusion capacitor C_s and the reset operation of readout amplifier circuit. The variance of reset noise can be expressed as:

$$\sigma^2_r = kTC_s/q^2, \tag{13}$$

where k is Boltzmann's constant, $k = 1.38054 \times 10^{-23}$; T is absolute temperature in Kelvin; q is the electronic charge, $q = 1.6 \times 10^{-19}$C [9], [20].

The CDS module, a part of a video processor, is used to treat the reset noise. It tends to sample the reference level and the signal level in one pixel cycle, respectively. Then the subtraction of twice sampling is taken as the valid signal. Because the noise sampling is of twice relevant, the noise can be eliminated [8], [9], [23], [24].

All the noises discussed above are independent, so the superposition of noises conforms to the principle of independent error synthesis. Except the noises that can be eliminated, the variance of the total noises of the sensor can be achieved:

$$\sigma_T^2 = \sigma_{photon}^2 + \sigma_{dark}^2, \tag{14}$$

where σ_{dark}^2 is the variance of dark current noise.

2) Noise of Imaging Circuit System: On the basis of the imaging system depicted in Fig. 2, the quality of the video signals output by TDI CCD relates to the driving circuits and the power circuits. Both circuits are desired to satisfy the operation conditions and requirements of TDI CCD, which can be fulfilled by reasonable design of the high-performance electronic devices, outputting driving signals with high integrity as expected timing sequence and stable bias voltages of low noise. Thus, their influence to the video signals can be negligible. The video signals, generated by the sensor, will pass through amplifiers and video processors. The noises of amplifiers mainly include thermal noise and 1/f noise. Both of them are minor and can be processed for suppression by CDS. The video processor is a bridge from analog signal to digital one, a key part for high SNR imaging, which is vulnerable to ground bounce noises. Besides this, there is quantization noise, so the noise of the video processor is mainly its working noise, denoted by σ_{ad}, which is zero mean and independent of the system output V_{DN}. Consequently, the noise of imaging circuit system primarily comes from video processors.

3) Noise Model of Imaging System: The output of TDI CCD is calculated according to (9) and put it into (12), then we can achieve the photon shot noise:

$$\sigma_{photon} = \sqrt{E(\lambda) M T_{INT} R(\lambda)}. \tag{15}$$

The noise is performed through the imaging system, finally displayed in the digital image. Thus, the photon shot noise of the imaging system in form of DN is:

$$\sigma_{sphoton} = G_{OP} G_{AD} k \sqrt{E(\lambda) M T_{INT} R(\lambda)}. \tag{16}$$

By the same principle, the dark current noise of the imaging system is:

$$\sigma_{sdark} = G_{OP} G_{AD} k \sigma_{dark}. \tag{17}$$

Using the principle of independent error synthesis, we can conclude the noise model of imaging system is:

$$\sigma_{sys}^2 = \sigma_{sphoton}^2 + \sigma_{sdark}^2 + \sigma_{ad}^2. \tag{18}$$

Put (16) and (17) into (18), and the theoretical noise model of the TDI CCD imaging system is:

$$\sigma_{\mathrm{sys}}^2 = \mathrm{G}_{\mathrm{OP}}^2 \mathrm{G}_{\mathrm{AD}}^2 \mathrm{k}^2 \mathrm{E}(\lambda) \mathrm{MT}_{\mathrm{INT}} \mathrm{R}(\lambda) + \mathrm{G}_{\mathrm{OP}}^2 \mathrm{G}_{\mathrm{AD}}^2 \mathrm{k}^2 \sigma_{\mathrm{dark}}^2 + \sigma_{\mathrm{ad}}^2. \tag{19}$$

Due to the response of imaging system shown as (10), we can obtain a formula with variable V_{DN}:

$$\sigma_{sys}^2 = G_{OP} G_{AD} k V_{DN} + G_{OP}^2 G_{AD}^2 k^2 \sigma_{dark}^2 + \sigma_{ad}^2. \tag{20}$$

So the variance of noise is linear with the output of imaging system. We can simplify (20) with parameters a and b, which can be applied as a priori information:

$$\sigma_{sys}^2 = a \times V_{DN} + b. \tag{21}$$

In which V_{DN} is the expectation of the intensity of pixels in the noisy image. Parameters a and b are to be estimated.

Consequently, the noise model of TDI CCD imaging system has the similar form with the conventional CCD or CMOS imaging system described in section II-A. It includes two items, the first item representing the signal-dependent noise(SD), the second item 'b' representing the signal-independent noise(SI). It is a Poissonian-Gaussian model. SD obeys the Poisson distribution, which is essentially due to the photon-counting process. SI obeys the Gauss distribution, because of electric and thermal noise added to the signal by the sensor's hardware [3], [11], [13], [16]. For the sake of simplification in [11], the usual normal approximation of the Poisson distribution is given:

$$\mathrm{P}(\lambda) \approx N(\lambda, \lambda).$$

The accuracy of this approximation increases with the parameter λ. In practice, for large enough λ, in other words, the number of incoming photons large enough, a Poissonian process can be treated as a special heteroskedastic Gaussian one described by [11] and [13]. So the noise distribution obeys the Gauss distribution in general.

When the video signal is near saturation, the response of the imaging system will tend to be uniform with the noise decreasing. Until full saturation, the system output in DN will be the maximum of the video processor. According to the analysis in section III-A-3), the output will reach (2^{n}-1) with uniform distribution and the noise will be zero. When there is no illumination, in particular, the system noise variance changes to the parameter b according to (21). The noise distribution becomes a shot noise instead of a Gaussian at this time, as [7] described. So the noise model is valid on the condition that the signal is not saturated. The establishment of the Gauss distribution of the noise is based on the assumptions that the signal is not saturated and the photon count is large enough.

IV. Proposed Method of Parameter Estimation

Compared with ML method, the LS has the advantages of easy implementation, simple algorithm and high efficiency, etc. So we focus on LS, based on which an improved method of parameter estimation is proposed. The thought of this method comes into being from weighted least square introduced in [12] and the curve fitting with piecewise linear function, called piecewise linear fitting(PLF), a method described in [25] for determining an optimal straight-line segment approximation to specified functions.

Let $y(t)$ be a real-valued function over the interval $[t_1, t_N]$, where t_1 and t_N are real numbers. It is desired to approximate $y(t)$ by $(N-1)$ connected straight line segments such that some performance index PI is minimized. The PI considered in [25] is:

$$PI = \int_{t_1}^{t_N} w(t)\,(y(t) - x(t))^2\,dt, \tag{22}$$

where $w(t)$ is a positive weighted function, and $x(t)$ is the piecewise linear function to approximate $y(t)$. Therefore, given $y(t)$, $w(t)$, N, t_1 and t_N, where $w(t)$ is set to 1 to get a simple form, using (22), we can find X and T to fit the function $y(t)$ accurately, where X and T are, respectively, the $N \times 1$ and $(N-2) \times 1$ column matrices defined by $X = [x_1\ x_2 \ldots x_N]^{\mathrm{T}}$ and $T = [t_2\ t_3 \ldots t_{N-1}]^{\mathrm{T}}$. So the fitting linear function can be expressed as:

$$x(t) = \frac{x_{i+1}(t - t_i) + x_i(t_{i+1} - t)}{(t_{i+1} - t_i)} \tag{23}$$

for $t_i \le t \le t_{i+1}$, $i = 1, 2, \ldots, N-1$. This piecewise linear fitting is an optimal method of curve approximation.

To implement accurate parameter estimation of noise curve, the piecewise weighted least square(PWLS) approach is proposed based on WLS and PLF, which integrates the advantages of both methods.

Unlike PLF in [25], the target function $y(t)$ and the number of breakpoints N are unknown in PWLS. Instead, we can acquire the data sets of the target function from experiments, set the number of internal split points, and seek the best ones on the condition of minimizing the SSE. Once knowing the locations of the split points, we can apply the WLS in each subinterval to realize the optimal fitting of the noise curve, achieving the straight line approximations at different areas. Thus, the core thought of PWLS is to fit the data by WLS in different subintervals using the linear expression, which makes the SSE minimum and obtains the accurate estimations of the parameters. A variable m is defined to describe the number of the internal split points during the interval, which indicates that there will be $(m+1)$ straight line segments to approximate the data sets.

The PWLS serves for sufficient discrete data sets and it is carried out as the specific procedures as follows:

1) Set the split point number m to 1, so the entire data sets are divided into two segments. And there should be two fitting lines.
2) Find the location of the split point based on LS. For the discrete data points $(x_i, y_i), i = 1 \ldots N$, we can find the best split point x_{b1} to make the SSE minimum. The expression of SSE is shown below:

$$x_{b1} = \arg\min_{x_{b1}}\Big(\sum_{i=1}^{b1}[\varphi_1(x_i) - y_i]^2 + \sum_{i=b1}^{N}[\varphi_2(x_i) - y_i]^2\Big), \tag{24}$$

   $2 \le b1 \le N-1$. $\varphi_1(x)$ is the linear fitting function of LS over the interval $[x_1, x_{b1}]$. $\varphi_2(x)$ is the one over the interval $[x_{b1}, x_N]$.
3) If the SSE meets the requirements or is small enough at the split point x_{b1}, i.e., SSE $< \varepsilon$, where ε is a positive given number depending on the specific application, we can gain two fitting lines based on LS over intervals $[x_1, x_{b1}]$ and $[x_{b1}, x_N]$. To further improve the estimation accuracy, the WLS is applied over each intervals.
4) The weighted factor W_i in [12] is not applicable here, because the number of points in each cluster is equal, resulting in the same W_i. So we need to design a new W_i. Firstly, the squared error between LS linear function and the data y_i is expressed as follows:

$$\Delta_i^2 = [\varphi_j(x_i) - y_i]^2,$$

   where $\varphi_j(x)$ is the LS linear function over subinterval j. Then the new W_i is defined by:

$$W_i = (\Delta_{max}^2 - \Delta_i^2)/\Delta_{max}^2, \tag{25}$$

   where Δ_{max}^2 is the maximum of Δ_i^2 over the subinterval. It is normalized in the range [0, 1], which can decrease the impact of large deviations. In particular, when Δ_i^2 equals Δ_{max}^2, W_i alters to zero; when the data points come close to the fitting line, W_i tends to be one.
5) So we can derive two linear expressions, using WLS, to fulfill the precise approximation. If the target function is linear, this fitting problem usually can be solved by one split point.
6) Else the SSE is not reasonable or not small enough, i.e., SSE $\ge \varepsilon$, we can find the best split points x_{b2} and x_{b3} over each intervals $[x_1, x_{b1}]$ and $[x_{b1}, x_N]$, similarly to step 2). The calculation formulas are given:

$$\begin{cases} x_{b2} = \arg\min\limits_{x_{b2}}\Big(\sum\limits_{i=1}^{b2}[\varphi_{11}(x_i) - y_i]^2 \\ \qquad\qquad + \sum\limits_{i=b2}^{b1}[\varphi_{12}(x_i) - y_i]^2\Big) \\ x_{b3} = \arg\min\limits_{x_{b3}}\Big(\sum\limits_{i=b1}^{b3}[\varphi_{21}(x_i) - y_i]^2 \\ \qquad\qquad + \sum\limits_{i=b3}^{N}[\varphi_{22}(x_i) - y_i]^2\Big). \end{cases} \tag{26}$$

   $\varphi_{11}(x)$ and $\varphi_{12}(x)$ are respectively the linear fitting function of LS over the subintervals $[x_1, x_{b2}]$ and $[x_{b2}, x_{b1}]$. $\varphi_{21}(x)$ and $\varphi_{22}(x)$ are respectively the one over the subintervals $[x_{b1}, x_{b3}]$ and $[x_{b3}, x_N]$.
7) If the sum of SSE of this two segments is reasonable, i.e., SSE $< \varepsilon$, we can obtain four fitting lines by applying WLS, as described in step 4), over each subintervals $[x_1, x_{b2}]$, $[x_{b2}, x_{b1}]$, $[x_{b1}, x_{b3}]$ and $[x_{b3}, x_N]$.
8) Else the SSE does not meet the requirements, i.e., SSE $\ge \varepsilon$, we can similarly find a series of split points x_{bi} to satisfy the required performance index by iteration. Thus, several fitting lines will be obtained by WLS over subintervals.

For the discrete data points $(x_i, y_i), i = 1 \ldots N$, the range of variable m is $[1, N-2]$, corresponding to two to $(N-1)$ fitting line segments. When $m = N-2$ and $W_i = 0$, there will

TABLE I
TECHNICAL SPECIFICATIONS OF THE IMAGING SYSTEM

Items	Specifications	
Spectral Range	P	450nm-800nm
	R	630nm-690nm
	G	520nm-600nm
	B	450nm-520nm
Pixel Size	P	8.75μm×8.75μm
	R, G, B	35μm×35μm
Spatial Pixels	P	4096
	R, G, B	1024
Optional Stages	P	8,16,32,48,72,96
	R	4,8
	G	4,8
	B	8,16
PGA	0dB-36dB	
Digital Resolution	10bits	

be $(N-1)$ line segments, the fitting problem changing into linear interpolation. When $m=0$, in particular, this parameter estimation method turns out to be WLS.

V. EVALUATION

A TDI CCD imaging system is developed, based on which a large number of image data are acquired. Using these data sets, we build a noise model with high precision, by which the method of parameter estimation is demonstrated and the theoretical noise model is verified in this section.

A. Experiment System

We develop an imaging system based on a TDI CCD sensor according to section III-A-2), which is capable of photosensitivity in four bands, i.e., panchromatic(P), red(R), green(G) and blue(B). The sensor requires 46 driving signals to implement the vertical transfer and horizontal readout of the pixels, and 6 kinds of bias voltages are needed. The vertical line rate for P spectrum is four times as the one for R, G and B due to their different pixels in size. The readout frequency for P, 7.5MHz, is twice as high as the one for R, G and B. The video processor can be fully programmable via a 3-wire serial interface, capable of sampling up to 40MHz. The range of its PGA is from 0dB to 36 dB, which can be set by the serial interface. The main technical specifications of the system are indicated in Table I and the architecture diagram of the sensor is depicted as Fig. 3. There are eight output ports for P spectrum, single one for each R, G and B spectrums.

The imaging experiments are set up to measure the precise relationship between the noise level and image intensity. This test system is constructed to implement the acquisition of multiple uniform images based on this TDI CCD imaging system, as shown in Fig. 4. We illuminate the sensor by uniform light source, capable to alter the brightness with the change of input voltage. To ensure constant-in-time(flicker-free) illumination, measurements are taken in a darkroom where the only source of light is an array of white LED lights supplied by stabilized DC power [26]. The imaging system is working under the setting parameters of the communication control system, which is in charge of the management and monitoring of the imaging system. The image data are

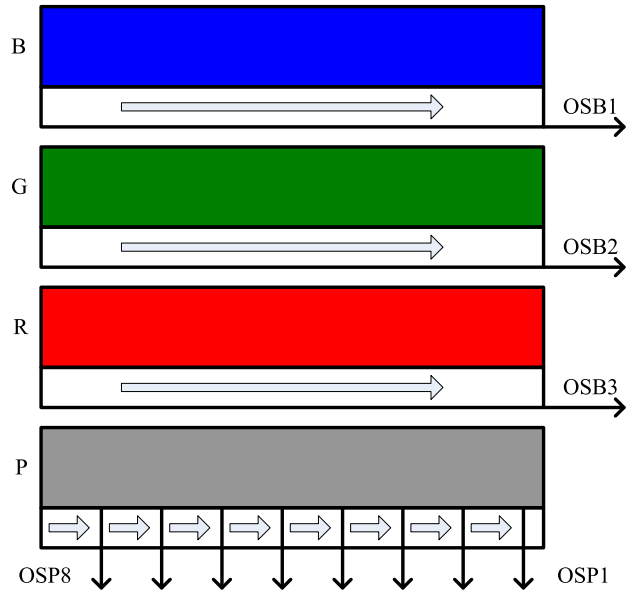

Fig. 3. Architecture diagram of the TDI CCD.

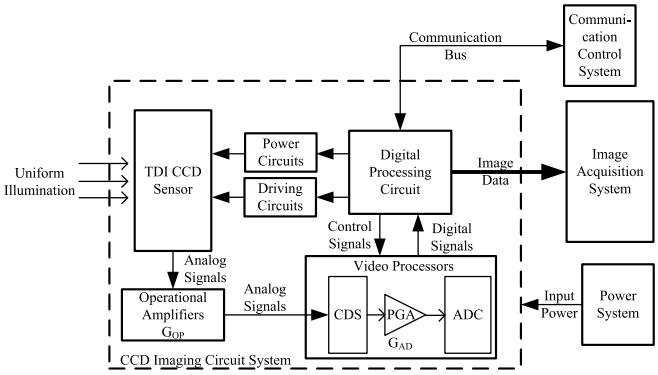

Fig. 4. Test block diagram of the imaging system.

captured by the image acquisition system, which can display and store the raw data. The power system supplies the whole imaging system.

We take a series of photographs toward different uniform illuminations to obtain the image data covering the whole range of the intensity by two sets of typical parameters, respectively. The first set of parameter(Para.1) is default, with which the imaging system will capture photos when powered on. It is 48 stages for P, 4 stages for R and G, 8 stages for B, integration time 105μs and magnification 1, simplified by 48-4-4-8-105μs-1X. To further validate the proposed estimation method and the theoretical model, we alter all the factors of the first set to 96-8-8-16-210μs-2X, the second set of parameter(Para.2). For a uniform field, the larger the data set from which the sample variance is computed, the closer to the real variance of the image [27]. Therefore, an image of dimension 512 columns $\times$ 1000 rows for each band is selected for calculation on each lighting condition. There are totally fourteen lighting conditions in each parameter state.

The estimation of expected intensity $\hat{\mu}_i$ and STD $\hat{\sigma}_i$ pairs can be directly calculated by (8) from the sufficient samples. So the statistical intensities of the raw image data are reported in Table II. For the raw data with 10-bit precision, the range

TABLE II
STATISTICAL RESULTS OF EXPECTED INTENSITY FOR EACH DATA SET

Sets	48-4-4-8-105μs-1X(Para.1)				96-8-8-16-210μs-2X(Para.2)			
	P	R	G	B	P	R	G	B
1	0.6	0.0	0.0	0.0	4.3	0.6	0.5	1.0
2	20.6	16.8	20.6	22.4	21.0	15.2	18.1	20.4
3	51.3	43.1	53.3	57.4	51.4	42.7	51.9	57.4
4	100.8	85.2	105.0	112.8	101.6	87.6	106.3	117.2
5	201.8	170.0	209.0	224.1	203.6	179.3	217.7	239.7
6	295.3	246.5	303.0	323.6	300.3	265.3	321.9	353.6
7	398.3	330.5	404.8	432.1	403. 6	352.3	432.2	470.3
8	498.1	413.2	505.5	538.4	502.3	436.2	535.0	581.1
9	593.5	496.0	605.5	643.4	600.5	520.0	637.0	691.0
10	698.3	592.7	721.6	764.9	701.3	605.3	740.4	802.6
11	789.6	685.1	831.0	877.3	802.4	690.7	844.4	914.0
12	893.5	799.3	963.3	1009.6	901.5	775.0	946.2	1021.1
13	996.1	922.2	1023.0	1023.0	1003.8	862.9	1023.0	1023.0
14	1023.0	992.5	1023.0	1023.0	1023.0	921.1	1023.0	1023.0

of the image intensity is [0, 1023]. All the images above are captured according to the pixel response of P spectrum, which are basically selected on equal interval principle by 100 DN, and the additive sets 2 and 3 are used to determine the noise curve in low response area precisely. The image data for R, G and B spectrums are acquired simultaneously.

B. Parameter Estimation and Data Analysis

According to the imaging principle of TDI CCD in section III-A-1), different column pixels output the video signal of the uniform target by cumulative exposure. So the uniformity along its columns is considerably more than the one along its rows [28]. Consequently, the data sets are analyzed by column.

Each data set corresponds to an image of dimension 512 columns $\times$ 1000 rows under one uniform illumination for the specific band, including hundreds of points, each representing the mean $\hat{\mu}$ and its variance $\hat{\sigma}^2$ for pixels of one column. For P spectrum, the data set can be denoted by x_P^j, which represents a set of points of P spectrum under the *j-th* illumination. Similarly, we can define $x_R^j, x_G^j,$ and x_B^j for R, G, and B spectrums, respectively. We can obtain fourteen data sets for fourteen kinds of illuminations, i.e., fourteen distinct clusters of points, so the range of variable j is [1,14].

The image data sets are usually analyzed by a scatter plot, a collection of points, each indicating image local mean versus local STD, i.e., $\{\hat{\mu}_i, \hat{\sigma}_i\}_{i=1}^N$ [10]–[13], [18], [19]. We can obtain the points with pairs $(\hat{\mu}_i, \hat{\sigma}_i)$ by computing the mean as the estimate of the intensity and the STD as that of the noise level for each column pixels of P, R, G and B channels. Fig. 5 describes the relationship between image intensity $\hat{\mu}$ and its variance $\hat{\sigma}^2$ in Para.1 state for the four bands. They can be fitted by linear expression. The variance grows with the increase of image intensity, but the speed of growth is changing. When it comes to the saturation area, the variance begins to decrease quickly to be zero. According to this characteristic, we can divide the noise curve into three segments: the low intensity area, high intensity area and saturation area.

From Table II and Fig. 5, we can see that the saturation area for P is X_P^{14} with their gray value being 1023 and variance being 0. There is no full saturation in R data sets, but X_R^{14} is significantly reducing compared with the previous data set X_R^{13}. So X_R^{14} belongs to the saturation area. For G band, there are two saturated data sets with their gray value being 1023 and variance being 0, i.e., X_G^{13} and X_G^{14}. Similarly to G band, there are two data sets of full saturation in B band, i.e., X_B^{13} and X_B^{14}. Besides them, X_B^{12} is significantly reducing to be zero. So the saturation area for B band includes X_B^{12}, X_B^{13} and X_B^{14}.

To accurately estimate the noise model except the saturation area, we exploit the PWLS approach, where the

TABLE III
SSE RESULTS FOR DIFFERENT SPLIT POINTS IN PARA.1 STATE

Band	*b1*	SSE for segment1 $X_P^1 - X_P^{b1}$	SSE for segment2 $X_P^{b1} - X_P^{13}$	SSE for both segments
P	2	3.0	3457.0	3460.0
	3	3.4	3322.0	3325.4
	4	4.6	3121.0	3125.6
	5	10.0	2802.0	2812.0
	6	13.8	2379.0	2392.8
	7	36.0	1748.0	1784.0
	8	49.2	1264.0	1313.2
	9	76.8	774.2	851.0
	10	**114.9**	**548.6**	**663.5**
	11	354.8	482.3	837.1
	12	1812.0	312.5	2124.5
R	*b1*	SSE for segment1 $X_R^1 - X_R^{b1}$	SSE for segment2 $X_R^{b1} - X_R^{13}$	SSE for both segments
	2	1.2	181.5	182.7
	3	3.7	162.0	165.7
	4	4.5	135.7	140.2
	5	10.4	116.3	126.7
	6	14.8	86.4	101.2
	7	20.1	70.4	90.5
	8	27.5	57.3	84.8
	9	**37.9**	**45.4**	**83.3**
	10	50.9	32.6	83.5
	11	73.2	23.9	97.1
	12	114.7	15.2	129.9
G	*b1*	SSE for segment1 $X_G^1 - X_G^{b1}$	SSE for segment2 $X_G^{b1} - X_G^{12}$	SSE for both segments
	2	0.4	197.0	197.4
	3	4.2	181.9	186.1
	4	6.9	159.0	165.9
	5	9.6	127.1	136.7
	6	13.6	107.0	120.6
	7	24.8	86.2	111.0
	8	36.0	48.4	84.4
	9	**43.5**	**30.8**	**74.3**
	10	80.0	25.3	105.3
	11	125.8	17.0	142.8
B	*b1*	SSE for segment1 $X_B^1 - X_B^{b1}$	SSE for segment2 $X_B^{b1} - X_B^{11}$	SSE for both segments
	2	1.1	143.9	145.0
	3	4.7	132.2	136.9
	4	8.4	115.4	123.8
	5	11.2	87.9	99.1
	6	**17.1**	**78.7**	**95.8**
	7	28.5	70.7	99.2
	8	40.7	57.6	98.3
	9	55.6	42.3	97.9
	10	83.6	25.5	109.1

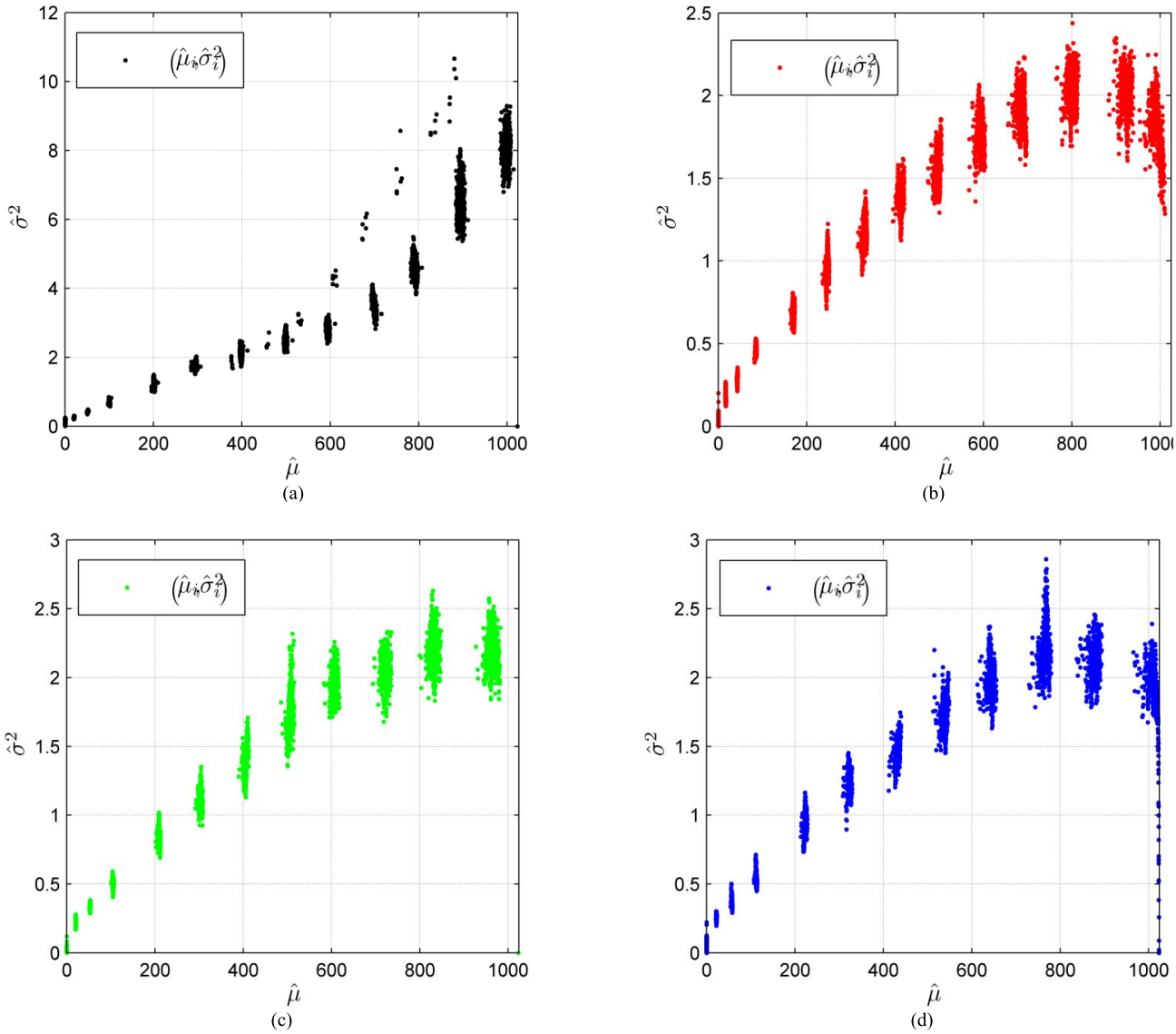

Fig. 5. Relationship between image intensity and its variance in Para.1 state. (a)-(d) Correspond to P, R, G and B spectrums, respectively.

split point number m is set to 1. The image data sets are analyzed and computed by Matlab tools. The location of the split point X_P^{b1} is determined in the light of the minimum SSE, $2 \leq b1 \leq 12 (X_P^{14}$ is saturated, so the linear data sets are $X_P^1 - X_P^{13})$, for P spectrum. Similarly, X_R^{b1}, X_G^{b1} and X_B^{b1} stand for the split points of R, G and B spectrums, respectively. For R, $2 \leq b1 \leq 12 (X_R^{14}$ is saturated); for G, $2 \leq b1 \leq 11 (X_G^{13}$ and X_G^{14} are saturated); for B, $2 \leq b1 \leq 10 (X_B^{12}, X_B^{13}$ and X_B^{14} are saturated). The solving process of the minimum SSE is shown in Table III.

So it has been seen that the locations of the split point for P, R, G and B bands are X_P^{10}, X_R^9, X_G^9 and X_B^6. Then the WLS is employed in each segment with the new weighted factor designed in section IV, e.g., $[X_P^1, X_P^{10}]$ and $[X_P^{10}, X_P^{13}]$ for P. To contrast the fitting effect, we also employ the WLS and the LS methods to estimate the noise model. The estimation results are plotted in Fig. 6.

We can see that the estimation result of WLS is close to that of LS, and both of them have large error, especially in low intensity, which even unreasonably appear negative value for the estimated $\hat{\sigma}$ in P spectrum. Instead, we replace the negative part with the line $\hat{\sigma} = 0$ to make it no less than zero.The PWLS fitting curve(red line) can pass through more data sets than the WLS and LS, indicating that it is more close to the actual value and a better estimation. The approximation results of the three methods are compared by the performance index SSE, RMSE(root of mean square error) and R-square(coefficient of determination), presented in Table IV.

The index R-square can measure how successful the fit is in explaining the variation of the data. A value closer to 1 indicates a better fit. So it can be seen that these data sets can be fitted by a linear expression through LS. The WLS approximates the data sets better than LS with a bigger R-square and smaller SSE and RMSE, using the weighted factors. The PWLS results have the smallest SSE and RMSE among them, so the fitting accuracy is the highest. The R-square is improved by different degrees, too. It is

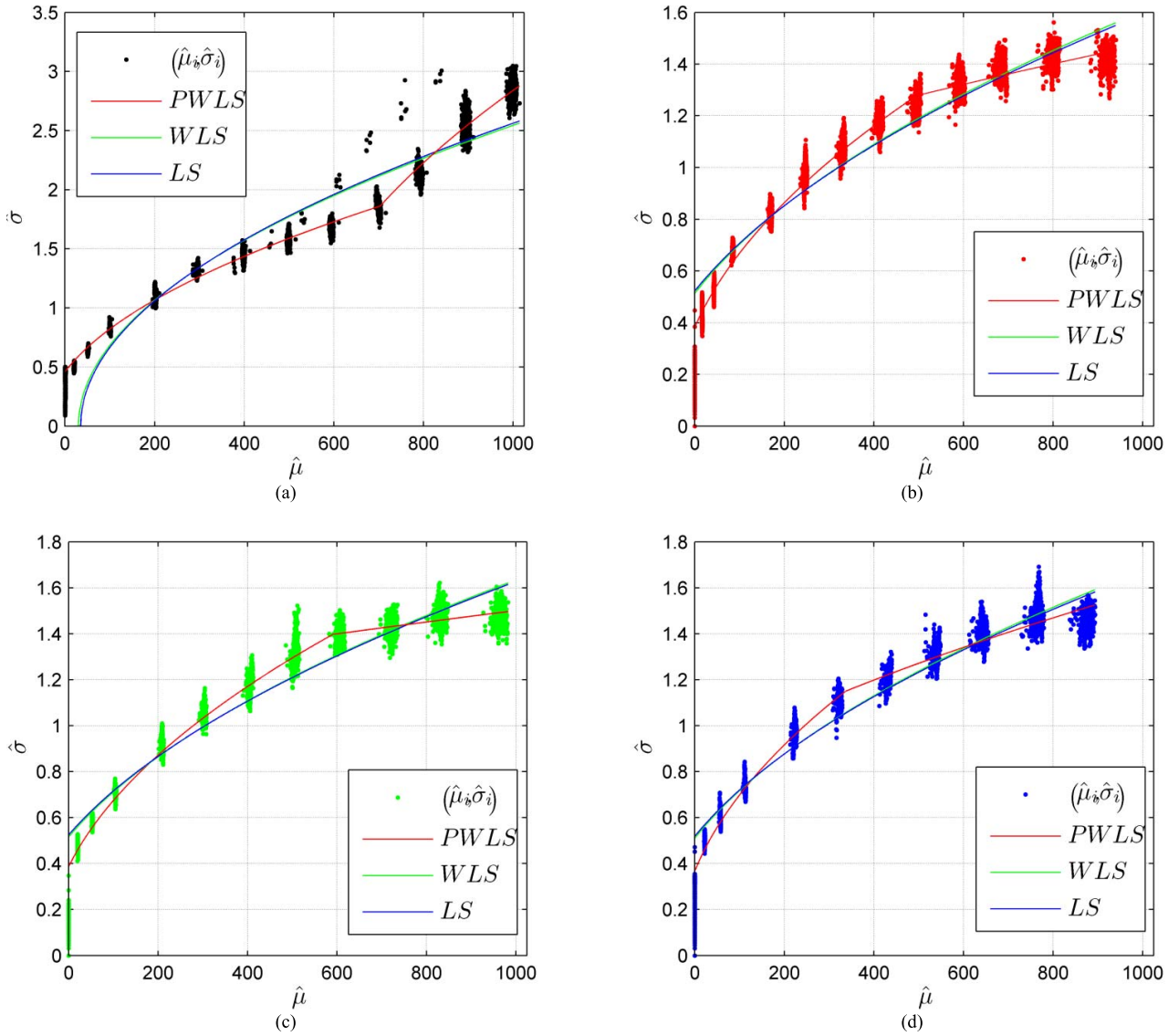

Fig. 6. Estimation curve of noise for each band in Para.1 state. (a)-(d) Correspond to P, R, G, and B spectrums. The red line, the green one and the blue one represent the approximation results of the three fitting methods, i.e., PWLS, WLS and LS, respectively.

TABLE IV

COMPARISON OF PERFORMANCE FOR THE THREE FITTING METHODS IN PARA.1 STATE

Band	Method	SSE	RMSE	R-square	
				Segment1	Segment2
P	PWLS	**475.9**	**0.2674**	**0.9835**	**0.9330**
	WLS	3000.0	0.6715	0.9113	
	LS	3546.0	0.7300	0.9060	
R	PWLS	**59.1**	**0.0949**	**0.9733**	0.6314
	WLS	178.7	0.1650	0.9406	
	LS	221.7	0.1838	0.9315	
G	PWLS	**57.0**	**0.0970**	**0.9793**	0.4230
	WLS	190.9	0.1775	0.9444	
	LS	241.0	0.1995	0.9349	
B	PWLS	**73.8**	**0.1153**	**0.9694**	0.8398
	WLS	134.6	0.1557	0.9538	
	LS	179.9	0.1800	0.9443	

TABLE V

COMPARISON OF PERFORMANCE FOR THE THREE FITTING METHODS IN PARA.2 STATE

Band	Method	SSE	RMSE	R-square	
				Segment1	Segment2
P	PWLS	**492.0**	**0.2830**	**0.9945**	0.9359
	WLS	666.0	0.3293	0.9885	
	LS	729.0	0.3445	0.9877	
R	PWLS	**337.5**	**0.2185**	0.9538	0.9352
	WLS	384.5	0.2332	**0.9822**	
	LS	443.7	0.2505	0.9801	
G	PWLS	**185.7**	**0.1751**	**0.9889**	0.8059
	WLS	274.8	0.2130	0.9877	
	LS	335.5	0.2353	0.9856	
B	PWLS	**144.7**	**0.1614**	**0.9926**	0.9235
	WLS	243.8	0.2096	0.9875	
	LS	289.2	0.2282	0.9858	

higher than WLS in segment1 for R, G and B bands and both segments for P. It decreases in segment2 for the three bands because of a certain degree of nonlinear feature in high intensity area. In spite of this, PWLS performs better than others with the minimum fitting deviation in general, providing higher precision.

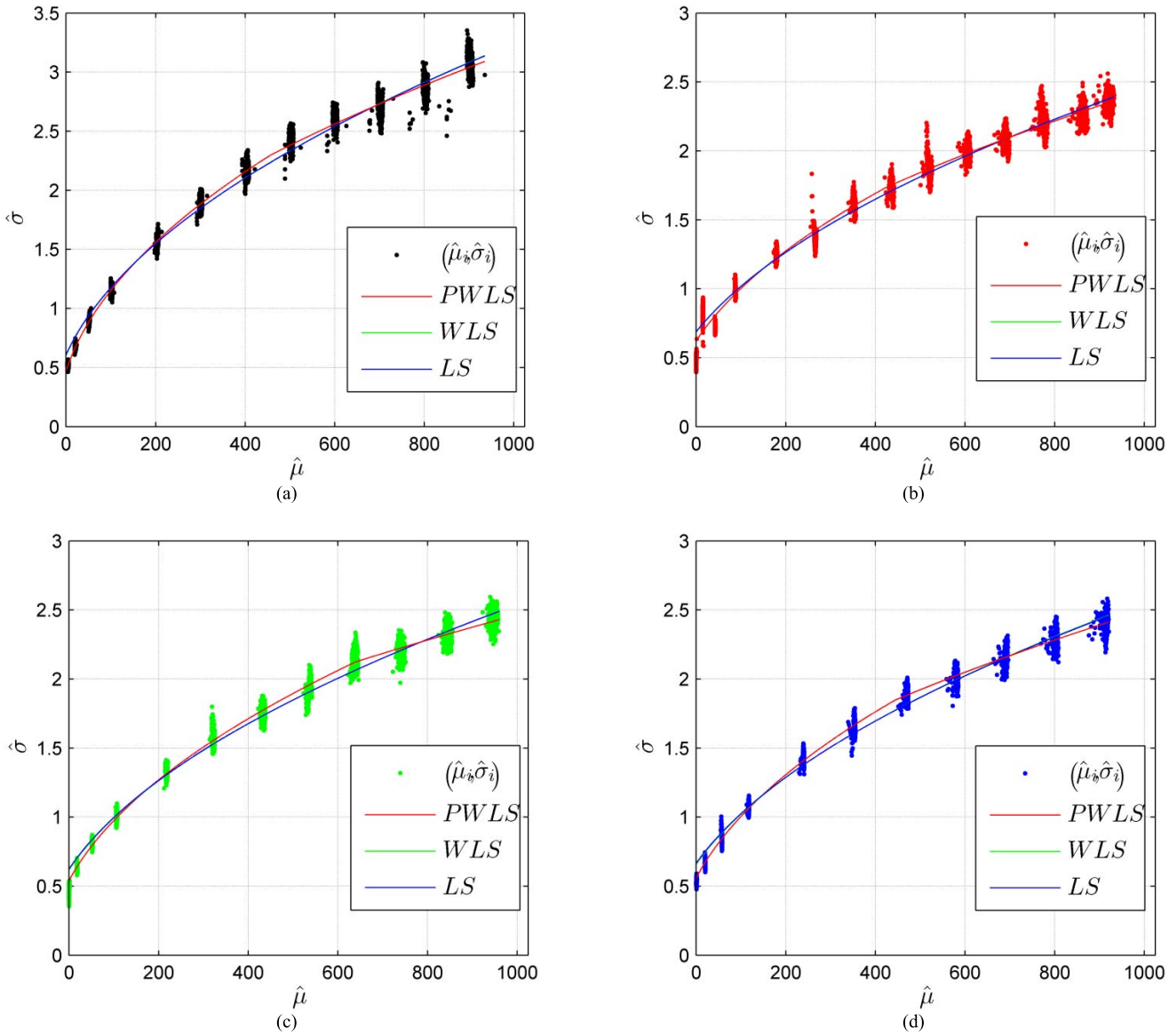

Fig. 7. Estimation curve of noise for each band in Para.2 state. (a)-(d) Correspond to P, R, G, and B spectrums. The red line, the green one and the blue one represent the approximation results of the three fitting methods, i.e., PWLS, WLS and LS, respectively.

Then we alter the imaging parameter to Para.2 to further validate the parameter estimation method. Employing the same procedures of processing and calculation, we can achieve the locations of the split point for P, R, G and B bands. Then the WLS is employed in each segment to obtain the estimated curve of PWLS. The estimation results in Para.2 state are plotted in Fig. 7. The comparison of performance for the three methods are reported in Table V.

According to Fig. 7 and Table V, we can draw a similar conclusion. The WLS approximates the raw data sets better than LS with a bigger R-square and smaller SSE and RMSE. The PWLS provides a higher-accuracy noise estimation than other methods with the minimum fitting deviation.

From Fig. 6 and Fig. 7, we can see that the noise level for R, G and B is lower than P band in both sets of parameters, due to the difference of the design of the pixels and their working conditions. The multispectral photosensitive area has bigger pixel size with larger full well voltage and its readout frequency is lower, half of the one in P. The noise level in Para.1 state for each band is lower than that in Para.2 state, because the factor G_{AD} in (20) changes to two times as the original. Although the same change has happened to the integration time and stages, they mainly affect the response of the system, i.e., the image intensity. In order to obtain a continuous noise curve, we choose two data areas with the overlapping data set to implement the PWLS, as shown in Table III. Once the two line segments are derived, there will be a cross point for them because of their different slopes. So the fitting noise curves are continuous presented in Fig. 6 and Fig. 7.

The PWLS performs better than other approximation methods no matter which set of parameters. We can obtain a high-precision estimation of the noise level by PWLS. Based on the analysis and outcomes above, it can be concluded that

TABLE VI
ESTIMATION RESULTS OF PWLS IN TWO PARAMETER STATES

Band	Intensity area	Para.1 state			
P	Low	$\hat{a}_1$	0.004625	$\hat{b}_1$	0.2114
	High	$\hat{a}_2$	0.015480	$\hat{b}_2$	-7.4170
R	Low	$\hat{a}_1$	0.003002	$\hat{b}_1$	0.1461
	High	$\hat{a}_2$	0.001082	$\hat{b}_2$	1.0970
G	Low	$\hat{a}_1$	0.003053	$\hat{b}_1$	0.1488
	High	$\hat{a}_2$	0.000744	$\hat{b}_2$	1.5180
B	Low	$\hat{a}_1$	0.003527	$\hat{b}_1$	0.1341
	High	$\hat{a}_2$	0.001803	$\hat{b}_2$	0.7150
Band	Intensity area	Para.2 state			
P	Low	$\hat{a}_1$	0.011070	$\hat{b}_1$	0.2235
	High	$\hat{a}_2$	0.008943	$\hat{b}_2$	1.1930
R	Low	$\hat{a}_1$	0.006193	$\hat{b}_1$	0.3845
	High	$\hat{a}_2$	0.005058	$\hat{b}_2$	0.8674
G	Low	$\hat{a}_1$	0.006603	$\hat{b}_1$	0.2899
	High	$\hat{a}_2$	0.004344	$\hat{b}_2$	1.7310
B	Low	$\hat{a}_1$	0.006985	$\hat{b}_1$	0.3097
	High	$\hat{a}_2$	0.005046	$\hat{b}_2$	1.1710

the PWLS method of parameter estimation is accurate, effective and practical. Certainly, more subdivisions will further improve the accuracy of noise estimations, but we believe the current segmentation algorithm is sufficient. So the estimation results of PWLS method for the noise model (21) in two parameter states are shown in Table VI.

Therefore, we can utilize the linear expressions to describe the function between the noise level and the pixel brightness based on LS fitting. Moreover, two piecewise linear expressions are derived with higher precision by PWLS. These analysis results validate the theoretical noise model established in section III-B-3), a linear model representing the relationship between the mean intensity and its variance.

This linear noise model discussed above can accurately estimate the noise level except the saturation area. The raw data captured by the TDI CCD imaging system are mainly at relatively low gray level, rather than the saturated one, which may lead to losing the effective target information. So it can play an important role in image preprocessing.

VI. CONCLUSION

In this paper, we have studied the noise model of a TDI CCD imaging system. The theoretical model is analyzed and established as a priori information. An improved method of parameter estimation is proposed, i.e., the PWLS. Through abundances of experiments on the developed imaging system, an accurate noise model is derived, validating the theoretical model and the proposed algorithm. The noise model can be utilized in a lot of image preprocessing. The PWLS method can provide a more accurate fitting and a better estimation. It can be extended to other type of sensors to obtain precise noise models and be applied to some other engineering fields, feasible to solve other fitting problems.

ACKNOWLEDGMENT

The authors would like to acknowledge the team of imaging electronics for their active involvements in the project.

REFERENCES

[1] S. Pyatykh, J. Hesser, and L. Zheng, "Image noise level estimation by principal component analysis," *IEEE Trans. Image Process.*, vol. 22, no. 2, pp. 687–699, Feb. 2013.
[2] A. Bosco, R. A. Bruna, D. Giacalone, S. Battiato, and R. Rizzo, "Signal-dependent raw image denoising using sensor noise characterization via multiple acquisitions," *Proc. SPIE*, vol. 7537, p. 753705, Jan. 2010.
[3] F. Luisier, T. Blu, and M. Unser, "Image denoising in mixed Poisson–Gaussian noise," *IEEE Trans. Image Process.*, vol. 20, no. 3, pp. 696–708, Mar. 2011.
[4] Y. Le Montagner, E. D. Angelini, and J.-C. Olivo-Marin, "An unbiased risk estimator for image denoising in the presence of mixed Poisson–Gaussian noise," *IEEE Trans. Image Process.*, vol. 23, no. 3, pp. 1255–1268, Mar. 2014.
[5] C. Liu, R. Szeliski, S. B. Kang, C. L. Zitnick, and W. T. Freeman, "Automatic estimation and removal of noise from a single image," *IEEE Trans. Pattern Anal. Mach. Intell.*, vol. 30, no. 2, pp. 299–314, Feb. 2008.
[6] C. Liu, W. T. Freeman, R. Szeliski, and S. B. Kang, "Noise estimation from a single image," in *Proc. IEEE Comput. Soc. Conf. Comput. Vis. Pattern Recognit.*, Jun. 2006, pp. 901–908.
[7] M. Colom, A. Buades, and J.-M. Morel, "Nonparametric noise estimation method for raw images," *J. Opt. Soc. Amer. A, Opt. Image Sci.*, vol. 31, no. 4, pp. 863–871, Apr. 2014.
[8] L.-P. Zhang, J.-Q. He, D. Hongliang, and C.-M. Wan, "Noise processing technology of a TDICCD sensor," in *Proc. IEEE Int. Conf. Comput., Mech. Control Electron. Eng. (CMCE)*, Aug. 2010, pp. 395–398.
[9] Y. Feng, X. Chen, X. Yang, and X. Yu, "Model of a TDI line scan camera and its electronics," in *Proc. IEEE 29th Annu. Conf. Ind. Electron. Soc.*, Nov. 2003, pp. 2215–2220.
[10] M. L. Uss, B. Vozel, V. V. Lukin, and K. Chehdi, "Image informative maps for component-wise estimating parameters of signal-dependent noise," *J. Electron. Imag.*, vol. 22, no. 1, p. 013019, Jan. 2013.
[11] A. Foi, M. Trimeche, V. Katkovnik, and K. Egiazarian, "Practical Poissonian–Gaussian noise modeling and fitting for single-image raw-data," *IEEE Trans. Image Process.*, vol. 17, no. 10, pp. 1737–1754, Oct. 2008.
[12] S. K. Abramov, V. Zabrodina, V. Lukin, B. Vozel, K. Chehdi, and J. Astola, "Improved method for blind estimation of the variance of mixed noise using weighted LMS line fitting algorithm," in *Proc. IEEE Int. Symp. Circuits Syst. (ISCAS)*, Jun. 2010, pp. 2642–2645.
[13] J. Meola, M. T. Eismann, R. L. Moses, and J. N. Ash, "Modeling and estimation of signal-dependent noise in hyperspectral imagery," *Appl. Opt.*, vol. 50, no. 21, pp. 3829–3846, Jul. 2011.
[14] Y. Tsin, V. Ramesh, and T. Kanade, "Statistical calibration of CCD imaging process," in *Proc. IEEE Int. Conf. Comput. Vis.*, Jul. 2001, pp. 480–487.
[15] G. E. Healey and R. Kondepudy, "Radiometric CCD camera calibration and noise estimation," *IEEE Trans. Pattern Anal. Mach. Intell.*, vol. 16, no. 3, pp. 267–276, Mar. 1994.
[16] S. Pyatykh and J. Hesser, "Image sensor noise parameter estimation by variance stabilization and normality assessment," *IEEE Trans. Image Process.*, vol. 23, no. 9, pp. 3990–3998, Sep. 2014.
[17] A. Foi, "Clipped noisy images: Heteroskedastic modeling and practical denoising," *Signal Process.*, vol. 89, no. 12, pp. 2609–2629, Dec. 2009.
[18] L. Alparone, M. Selva, L. Capobianco, S. Moretti, L. Chiarantini, and F. Butera, "Quality assessment of data products from a new generation airborne imaging spectrometer," in *Proc. IEEE Int. Geosci. Remote Sens. Symp.*, Cape Town, Southern Africa, Jul. 2009, pp. 422–425.
[19] V. V. Lukin *et al.*, "Methods and automatic procedures for processing images based on blind evaluation of noise type and characteristics," *J. Appl. Remote Sens.*, vol. 5, no. 1, p. 053502, Jan. 2011.
[20] Y.-X. Liu and Z.-H. Hao, "Research on the nonuniformity correction of linear TDI CCD remote camera," *Proc. SPIE*, vol. 5633, pp. 527–535, Jan. 2005.
[21] R. Widenhorn, M. M. Blouke, A. Weber, A. Rest, and E. Bodegom, "Temperature dependence of dark current in a CCD," *Proc. SPIE*, vol. 4669, pp. 193–201, Apr. 2002.

[22] R. Widenhorn, J. C. Dunlap, and E. Bodegom, "Exposure time dependence of dark current in CCD imagers," *IEEE Trans. Electron Devices*, vol. 57, no. 3, pp. 581–587, Mar. 2010.
[23] D. He, J. Zhou, C. Liu, and H. Chen, "Research into multispectral TDI-CCD imaging and fusion technology," *Proc. SPIE*, vol. 10025, p. 100251L, Nov. 2016.
[24] R. Yu, Y. Liu, and J. Lu, "Design of a TDI CCD data acquisition system," in *Proc. 5th Int. Conf. Biomed. Eng. Inform. (BMEI)*, Oct. 2012, pp. 735–738.
[25] A. Cantoni, "Optimal curve fitting with piecewise linear functions," *IEEE Trans. Comput.*, vol. C-20, no. 1, pp. 59–67, Jan. 1971.
[26] A. Foi, S. Alenius, V. Katkovnik, and K. Egiazarian, "Noise measurement for raw-data of digital imaging sensors by automatic segmentation of nonuniform targets," *IEEE Sensors J.*, vol. 7, no. 10, pp. 1456–1461, Oct. 2007.
[27] P. Meer, J. Jolion, and A. Rosenfeld, "A fast parallel algorithm for blind estimation of noise variance," *IEEE Trans. Pattern Anal. Mach. Intell.*, vol. 12, no. 2, pp. 216–223, Feb. 1990.
[28] B. M. Ratliff and J. R. Kaufman, "Scene-based correction of fixed pattern noise in hyperspectral image data using temporal reordering," *Opt. Eng.*, vol. 54, no. 9, p. 093102, Sep. 2015.

Liangliang Zheng received the B.S. and M.S. degrees in mechanical and electronic engineering from the Nanjing University of Aeronautics and Astronautics, Nanjing, China, in 2005 and 2007, respectively. He is currently pursuing the Ph.D. degree in optical engineering with the University of Chinese Academy of Sciences, Beijing, China.

Since 2007, he has been with the Changchun Institute of Optics, Fine Mechanics and Physics, Chinese Academy of Sciences, Changchun, China, where he is currently an Associate Research Fellow. His research interest includes the digital image processing and space-borne imaging technology of high SNR.

Guang Jin received the B.S. degree in optical instrument from the Changchun College of Optics and Fine Mechanics, Changchun, China, in 1982, and the M.S. and Ph.D. degrees in optical engineering from the Changchun Institute of Optics, Fine Mechanics and Physics, Chinese Academy of Sciences, Changchun, China, in 1991 and 2001, respectively.

He has been with the Changchun Institute of Optics, Fine Mechanics and Physics, Chinese Academy of Sciences, Changchun, China, since 1991, where he currently a Research Fellow and a Doctoral Supervisor in optical engineering. His current research interest includes the space optical remote sensing and system technology of small satellites.

Wei Xu received the B.S. degree in mechanical and electronic engineering from Jilin University, Changchun, China, in 2003, and the Ph.D. degree in mechanical and electronic engineering from the Changchun Institute of Optics, Fine Mechanics and Physics, Chinese Academy of Sciences, Changchun, China, in 2008.

After graduation, he worked at the Changchun Institute of Optics, Fine Mechanics and Physics, Chinese Academy of Sciences, Changchun, China. Now, he is a Research Fellow and a Doctoral Supervisor. His current research interests include the integration technology of satellites and payloads and the high reliable electronic systems for aerospace.

Hongsong Qu received the B.S. degree in mechanical and electronic engineering from Jilin University, Changchun, China, in 2003, and the Ph.D. degree in mechanical and electronic engineering from the Changchun Institute of Optics, Fine Mechanics and Physics, Chinese Academy of Sciences, Changchun, China, in 2008.

He stayed and worked at the Changchun Institute of Optics, Fine Mechanics and Physics, Chinese Academy of Sciences, Changchun, China. And now he is a Research Fellow. His current research interest lies in the space-borne camera system technology.

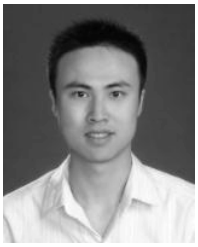

Yong Wu received the B.S. degree in survey and control technology and instrument and the M.S. degree in instrument science and technology from Jilin University, Changchun, China, in 2011 and 2014, respectively.

After graduation, he worked at the Changchun Institute of Optics, Fine Mechanics and Physics, Chinese Academy of Sciences, Changchun, China. And now he is an Assistant Researcher. His current research interest is the electronic systems of space-borne cameras.